Dynamics of twin pulse propagation and dual-optical switching in a Λ + Ξ atomic medium

Hoang Minh Dong [a,*], Nguyen Thi Thu Hien [a,b], Nguyen Huy Bang [b], Le Van Doai [b,*]

[a] *Ho Chi Minh City University of Industry and Trade, Ho Chi Minh City, Viet Nam*
[b] *Vinh University, 182 Le Duan Street, Vinh City, Viet Nam*

A R T I C L E   I N F O

A B S T R A C T

Optical bistability (OB) and optical multistability (OM) as well as optical soliton and all-optical switching have been successfully established in a lambda + cascade-type five-level atomic medium under electromagnetically induced transparency (EIT) and electromagnetically induced absorption (EIA) regimes. For this configuration, three laser fields are required to excite atomic transitions. The probe laser field with two circularly left- and right-polarized components excites atoms in a lambda-type configuration. Meanwhile, two coupling laser fields excite atoms in a ladder-type configuration. In this way, the above optical phenomena can occur with two frequency channels corresponding to the circularly left- and right-polarized light components. By adjusting the strength/ direction of the static magnetic field in the presence of the driving field, the EIT and EIA effects can be swapped, at the same time, OB and OM effects can also be converted. In the EIT regime, the propagation of the probe pulse easily achieves the soliton state, whereas it can be completely extinguished in the EIA regime. This makes it easy to create an all-optical switching mechanism. Especially, both components of the probe field (cw) can be modulated into a synchronous or asynchronous square pulse according to the modulation of the driving field. The results obtained from the investigated model may provide merits of the applications for optical storage and all-optical switching for multi-channel optical communications.

1. Introduction

Optical solitons and all-optical switches play a crucial role in high-speed optical communication networks and optical storage devices [1,2]. The theoretical models of optical soliton and optical switches can refer to Refs. [3–7]. In recent years, researchers have been actively seeking materials that can create optical switching with controllable characteristics, high switching speeds, and low-threshold optical solitons. Nevertheless, saturation effects are an enormous obstacle to achieving these properties in conventional nonlinear materials. To overcome this, electromagnetically induced transparency (EIT) has emerged as an excellent solution to suppress saturation effects [8]. The EIT material possesses not only reduced absorption but also giant nonlinearity in the vicinity of atomic resonance frequency [9–12]. As a result, a lot of nonlinear optical effects can be observed with very low light intensities, even with a single photon [13–15]. Furthermore, the variable nonlinearity of EIT materials has also provided a simple method to control both the threshold intensity and the width of optical bist-ability (OB) as well as all-optical switching (AOS) by external fields

[16,17]. Early theoretical and experimental studies of OB were focused on simple three-level atomic systems consisting of three-level lambda-, V-, and ladder-type structures [18–22]. These studies revealed that the threshold intensity and the width of the OB system can be effectively controlled by adjusting the intensity and the frequency of the laser fields. In particular, thanks to the giant and changeable nonlinearity of EIT materials, optical multistability (OM) is also easily achieved with three-level and four-level atomic configurations [23–27]. The underly-ing mechanism of OB is fundamental to applications in all-optical switches, storage, and optical memory [28,29].

In addition to the typical steady-state optical properties above, the dynamic optical properties of EIT materials are also exploited to create optical solitons with low threshold intensity and variable characteristics [30]. On the other hand, the propagation of laser pulses as optical sol-itons in the EIT regime or completely absorbed by the medium in the EIA regime is the basis for creating all-optical switching with ultrahigh switching speeds [31–36]. Indeed, Schmidt et al. [37] introduced an all-optical switching method based on absorption modulation in a three-level Λ-type atomic system. Yavuz et al. [38] proposed a technique for

* Corresponding authors.
E-mail addresses: dong.gtvtmt@gmail.com (H.M. Dong), doailv@vinhuni.edu.vn (L. Van Doai).
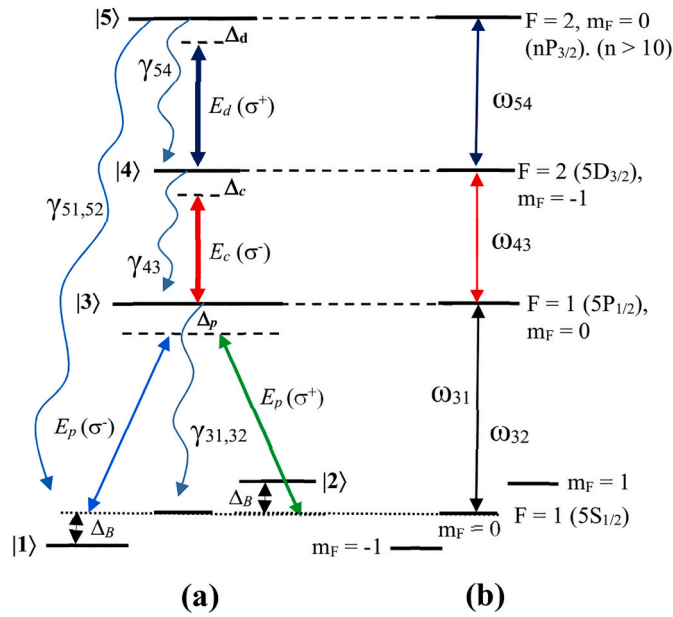
Fig. 1. (a) The $\Lambda + \Xi$-type five-level atomic scheme in the presence of a static magnetic field. Under a static magnetic field parallel to the propagation direction of the laser fields, the level $|1\rangle$ is lowered while the level $|2\rangle$ is lifted by the same amount Δ_B corresponding to the Zeeman shift. The symbols Δ_p, Δ_c, and Δ_d are the frequency detunings of the corresponding probe, control, and driving beams, respectively. (b) Relevant energy levels of ^{87}Rb atom and excitations of the laser fields in the experimental realization.

complete optical conversion using two-photon absorption in a three-level Λ-type atomic system. Antón et al. [39] achieved all-optical switching in a five-level N-tripod-type atom. Yang et al. [40] used a radio field to control the propagation dynamic and all-optical switching in a four-level atomic system. Paspalakis et al. [41] investigated the implementation of all-optical modulation in three-level lambda-type quantum systems and demonstrated its dependence on the applied laser field and atomic parameters. Qi et al. [42] showed that the switching action of the probe laser pulse can be realized by adjusting the phase or the intensity of the coupling fields in a four-level atomic system [43]. Yu et al. [44] presented the pulse propagation and all-optical switching in a five-level double-ladder atom medium. Ma et al. [45] created ultrahigh efficiency all-optical switching and ultralow threshold energy using a PT-symmetric waveguide structure. Most recently, Dong et al. [46–50] have presented optical switching based on quantum coherent and external magnetic fields. The above studies have shown a close relationship between OB and AOS effects and optical soliton, so a simultaneous study of these phenomena in EIT materials may prove the merits of the applications for modern photonic devices.

In this work, we realize EIT-based OB and OM effects, optical soliton, and all-optical switching in a lambda + cascade-type ($\Lambda + \Xi$-type) five-level atomic medium by numerically solving coupled Maxwell-Bloch equations on a space-time grid. The transition between EIT and EIA regimes in this atomic configuration can be achieved by turning the parameters of the driving lasers and/or the external magnetic field. Such variable optical properties of the medium are used to implement OB and OM effects in the steady-state, as well as optical solitons and optical switching in the dynamic propagation regime. Another exciting motivation in this paper is that two components of opposite circular polarization (σ^- and σ^+) from a linearly-polarized probe beam at different frequencies can be switched on or off by a single driving beam.

2. Model and basic equations

We consider a $\Lambda + \Xi$ configuration five-level atomic scheme as

depicted in Fig. 1. In this configuration, the two lower states, denoted as $|1\rangle$ and $|2\rangle$, represent degenerate Zeeman sublevels corresponding respectively to the magnetic quantum numbers $m_F = 1$ and $m_F = -1$ of a ground-state hyperfine level F = 1 [28,44]. The three upper states, namely $|3\rangle$, $|4\rangle$, and $|5\rangle$, represent the Zeeman sublevels of different excited states. These upper states belong to hyperfine levels where electric dipole transitions are permitted [see Fig. 1(b)]. Within this setup, the medium is subject to a longitudinal magnetic field B, which removes the degeneracy of the ground-state sublevels $|1\rangle$ ($m_F = -1$) and $|2\rangle$ ($m_F = +1$). The Zeeman shift of the levels $|1\rangle$ and $|2\rangle$ is given by $\Delta_B = \mu_B m_F g_F B/\hbar$, where μ_B and g_F are the Bohr magneton and the Landé factors and $m_F = \pm 1$ is the magnetic quantum number of the corresponding state. The probe laser field (with the carrier frequency ω_p and electric field amplitude E_p) includes two circularly left-E_{p-} and right-E_{p+} polarized components, which interact with the transitions $|3\rangle \leftrightarrow |1\rangle$ and $|3\rangle \leftrightarrow |2\rangle$, respectively [23,38,45]. The transition $|3\rangle \leftrightarrow |4\rangle$ is coupled by the strong control laser field with the carrier frequency ω_c and electric field amplitude E_c. The transition $|4\rangle \leftrightarrow |5\rangle$ is controlled by the driving laser field with the carrier frequency ω_d and electric field amplitude E_d. All laser fields are oriented parallel to the direction of the static magnetic field. The Rabi frequency of laser fields is related to the corresponding electric field amplitude as $2\Omega_p^- = \mu_{31}E_p^-/\hbar$ ($2\Omega_p^+ = \mu_{32}E_p^+/\hbar$), $2\Omega_c = \mu_{43}E_c/\hbar$ and $2\Omega_d = \mu_{54}E_d/\hbar$, here, μ_{ij} denotes the electric-dipole moment for the atomic transition between the levels $|i\rangle$ and $|j\rangle$. We define $\Delta_p = \omega_{31} - \omega_p - \Delta_B = \omega_{32} - \omega_p + \Delta_B$, $\Delta_c = \omega_{43} - \omega_c$, and $\Delta_d = \omega_{54} - \omega_d$ are the frequency detunings of the probe, control, and driving fields from the corresponding atomic transitions. We denote γ_{ij} is the decay rate between levels $|i\rangle$ and $|j\rangle$. The relaxation rates of atomic coherence between the ground states $|1\rangle$ and $|2\rangle$ by collisions are negligible for the cold atomic medium, so that they can be omitted.

Using the electric dipole and the rotating-wave approximations, the interaction Hamiltonian of the system can be given by (assuming $\hbar = 1$) [44]:

$$H_{\text{int}} = \begin{bmatrix} 0 & 0 & -\Omega_{p-} & 0 & 0 \\ 0 & 2\Delta_B & -\Omega_{p+} & -\Omega_s & 0 \\ -\Omega_{p-}^* & -\Omega_{p+}^* & \Delta_p + \Delta_B & -\Omega_c & 0 \\ 0 & 0 & -\Omega_c^* & \Delta_1 & -\Omega_d \\ 0 & 0 & 0 & -\Omega_d^* & \Delta_2 \end{bmatrix}. \tag{1}$$

where $\Delta_1 = \Delta_p + \Delta_c + \Delta_B$ and $\Delta_2 = \Delta_p + \Delta_c + \Delta_d + \Delta_B$. and Δ_B is the Zeeman shift of the levels $|1\rangle$ and $|2\rangle$ when the magnetic field is activated, and Δ_B is taken to zero for a zero magnetic field.

To describe the dynamical evolution of the proposed system, the density matrix approach is employed via Liouville equation:

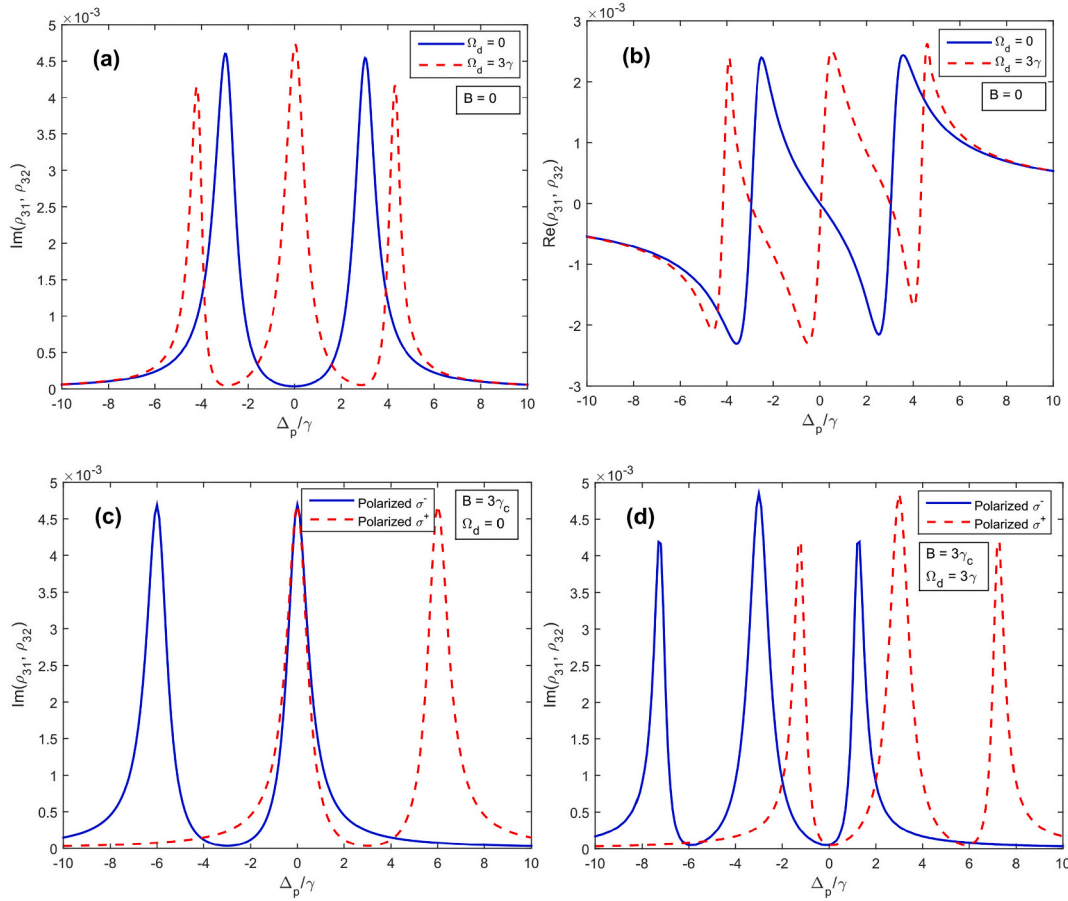$$\frac{\partial \rho}{\partial t} = -i[H_{\text{int}}, \rho] + \Lambda\rho, \tag{2}$$

where the term $\Lambda\rho$ represents the decay part in the atom, with Λ is the Liouvillian operator acting on the density matrix ρ. Using Eqs. (1) and (2), the density matrix equations of motion are written as:

$$\dot{\rho}_{11} = \gamma_{31}\rho_{33} + \gamma_{51}\rho_{55} - i\Omega_{p-}\rho_{13} + i\Omega_{p-}^*\rho_{31}, \tag{3a}$$

$$\dot{\rho}_{22} = \gamma_{32}\rho_{33} + \gamma_{52}\rho_{55} - i\Omega_{p+}\rho_{23} + i\Omega_{p+}^*\rho_{32}, \tag{3b}$$

$$\begin{aligned}\dot{\rho}_{33} = &-(\gamma_{31} + \gamma_{32})\rho_{33} + \gamma_{43}\rho_{44} + i\Omega_{p-}\rho_{13} - i\Omega_{p-}^*\rho_{31} + i\Omega_{p+}\rho_{23} - i\Omega_{p+}^*\rho_{32} \\ &- i\Omega_c\rho_{34} + i\Omega_c^*\rho_{43},\end{aligned} \tag{3c}$$

$$\dot{\rho}_{44} = -\gamma_{43}\rho_{44} + \gamma_{54}\rho_{55} - i\Omega_c^*\rho_{43} + i\Omega_c\rho_{34} - i\Omega_d\rho_{45} + i\Omega_d^*\rho_{54}, \tag{3d}$$

Fig. 2. The absorption and dispersion coefficients versus the probe detuning at the B = 0 when the driving field is turned off $\Omega_d = 0$ or on $\Omega_d = 3\gamma$ [panels (a) and (b)]. The absorption coefficient of two circularly polarized components versus the probe detuning at the B = $3\gamma_c$ when the driving field is turned off $\Omega_d = 0$ [panel (c)] and turned on $\Omega_d = 3\gamma$ [panel (d)]. The other parameters are given by $\Omega_p = 0.01\gamma$, $\Omega_c = 3\gamma$, and $\Delta_c = \Delta_d = 0$, respectively.

$$\dot{\rho}_{55} = -(\gamma_{51} + \gamma_{52} + \gamma_{54})\rho_{55} + i\Omega_d\rho_{45} - i\Omega_d^*\rho_{54}, \tag{3e}$$

$$\dot{\rho}_{21} = -2i\Delta_B\rho_{21} - i\Omega_{p-}\rho_{23} + i\Omega_{p+}^*\rho_{31}, \tag{3f}$$

$$\dot{\rho}_{31} = -\left(i(\Delta_p + \Delta_B) + \frac{\gamma_{31} + \gamma_{32}}{2}\right)\rho_{31} - i\Omega_{p-}(\rho_{33} - \rho_{11}) + i\Omega_{p+}\rho_{21} + i\Omega_c^*\rho_{41}, \tag{3g}$$

$$\dot{\rho}_{41} = -\left(i\Delta_1 + \frac{\gamma_{43}}{2}\right)\rho_{41} - i\Omega_{p-}\rho_{43} + i\Omega_c\rho_{31} + i\Omega_d^*\rho_{51}, \tag{3h}$$

$$\dot{\rho}_{51} = -\left(i\Delta_2 + \frac{\gamma_{51} + \gamma_{52} + \gamma_{54}}{2}\right)\rho_{51} - i\Omega_{p-}\rho_{53} + i\Omega_d\rho_{41}, \tag{3i}$$

$$\dot{\rho}_{32} = -\left(i(\Delta_p - \Delta_B) + \frac{\gamma_{31} + \gamma_{32}}{2}\right)\rho_{32} - i\Omega_{p+}(\rho_{33} - \rho_{22}) + i\Omega_{p-}\rho_{12} + i\Omega_c^*\rho_{42}, \tag{3k}$$

$$\dot{\rho}_{42} = -\left(i(\Delta_p + \Delta_c - \Delta_B) + \frac{\gamma_{43}}{2}\right)\rho_{42} - i\Omega_{p+}\rho_{43} + i\Omega_c\rho_{32} + i\Omega_d^*\rho_{52}, \tag{3l}$$

$$\dot{\rho}_{52} = -\left(i(\Delta_p - \Delta_B + \Delta_c + \Delta_d) + \frac{\gamma_{51} + \gamma_{52} + \gamma_{54}}{2}\right)\rho_{52} - i\Omega_{p+}\rho_{53} + i\Omega_d\rho_{42}, \tag{3m}$$

$$\dot{\rho}_{43} = -\left(i\Delta_c + \frac{\gamma_{31} + \gamma_{32} + \gamma_{43}}{2}\right)\rho_{43} - i\Omega_c(\rho_{44} - \rho_{33}) - i\Omega_{p-}^*\rho_{41} - i\Omega_{p+}^*\rho_{42} + i\Omega_d^*\rho_{53}, \tag{3n}$$

$$\dot{\rho}_{53} = -\left(i(\Delta_c + \Delta_d) + \frac{\gamma_{31} + \gamma_{32} + \gamma_{51} + \gamma_{52} + \gamma_{54}}{2}\right)\rho_{53} - i\Omega_{p-}^*\rho_{51} - i\Omega_{p+}^*\rho_{52} - i\Omega_c\rho_{54} + i\Omega_d\rho_{43}, \tag{3o}$$

$$\dot{\rho}_{54} = -\left(i\Delta_d + \frac{\gamma_{51} + \gamma_{52} + \gamma_{54} + \gamma_{43}}{2}\right)\rho_{54} - i\Omega_c^*\rho_{53} - i\Omega_d(\rho_{55} - \rho_{44}), \tag{3p}$$

where, $\rho_{11} + \rho_{22} + \rho_{33} + \rho_{44} + \rho_{55} = 1$ and $\rho_{ij} = \rho_{ji}^*$, and γ_{ij} is the decay rate between levels $|i\rangle$ and $|j\rangle$, respectively.

3. Results and discussion

In the investigations below, we apply the $\Lambda + \Xi$-type five-level scheme to the ^{87}Rb cold atom on the $5S_{1/2} - 5P_{1/2} - 5D_{3/2} - nP_{3/2}$ (n > 10) transitions. The detailed coupling diagram is found in Fig. 1(a), corresponding to the states [44,51]: $|1\rangle = |5S_{1/2}, F = 1, m_F = -1\rangle$, $|2\rangle = |5S_{1/2}, F = 1, m_F = +1\rangle$, $|3\rangle = |5P_{1/2}, F = 1, m_F = 0\rangle$, $|4\rangle = |5D_{3/2}, F = 2, m_F = -1\rangle$, $|5\rangle = |nP_{3/2}, F = 0, m_F = 0\rangle$, respectively. The atomic parameters are selected as: $\gamma_{31} = \gamma_{32} = 2\pi \times 5.3$ MHz, $\gamma_{43} \simeq 2\pi \times 0.67$ MHz, $\gamma_{51} = \gamma_{52} = \gamma_{54} \simeq 2\pi \times 0.09$ MHz, $N = 4.5 \times 10^{17}$ atoms/m^3, $\mu_{31} = 1.6 \times 10^{-29}$ C.m, $g_F = -1/2$ and $\mu_B = 9.27401 \times 10^{-24}$ JT^{-1}. Here, the Zeeman shift Δ_B is taken in terms of decay rate γ_{31}, so the strength of the magnetic field B is in terms of the unit of the combined constant $\gamma_c = \hbar\gamma_{31}/(\mu_B g_F)$. For simplicity in numerical simulation, the quantities in frequency units can be normalized by $\gamma = \gamma_{31}$.
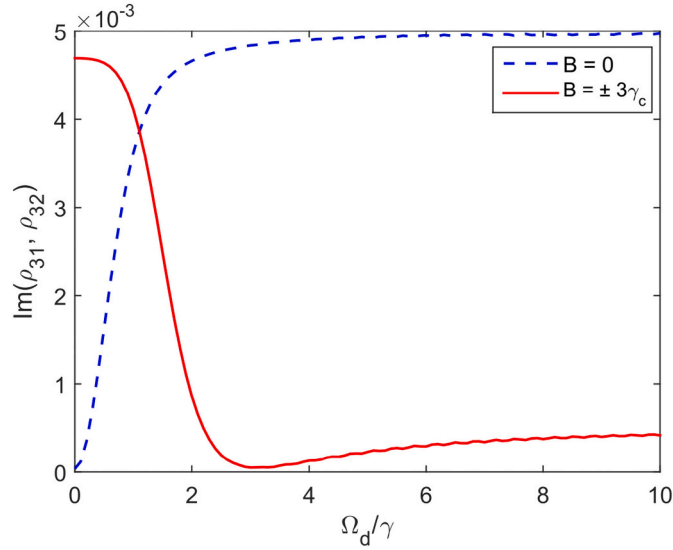
Fig. 3. (a) Graph of the absorption coefficients Im(ρ_{31}, ρ_{32}) versus the driving field Ω_d at $\Delta_p = 0$, when magnetic field off B = 0 (blue dashed line) and B = $\pm 3\gamma_c$ (red solid line). The other parameters are given by $\Omega_p = 0.01\gamma$, $\Omega_c = 3\gamma$, and $\Delta_c = \Delta_d = 0$, respectively. (For interpretation of the references to color in this figure legend, the reader is referred to the web version of this article.)

3.1. Variable absorption and dispersion properties

To start with, we analytically solve the density matrix equations in steady-state to find the solutions of ρ_{31} and ρ_{32} corresponding to the atomic response for the probe polarization components. For the initial condition, we assume that all atoms are in the ground states $|1\rangle$ and $|2\rangle$ with the same populations, namely $\rho_{11} = \rho_{22} = 1/2$ while $\rho_{33} = \rho_{44} = \rho_{55} = 0$ [28,44]. Under the weak-probe field approximation, the analytical expressions of the coherences ρ_{31} and ρ_{32} are obtained as:

$$\rho_{31,\ 32} = \frac{i\Omega_{p-,+}}{2}\left(\frac{bc + |\Omega_d|^2}{abc + c|\Omega_c|^2 + a|\Omega_d|^2}\right),\tag{4}$$

where $a = i(\Delta_p \pm \Delta_B) + \frac{\gamma_{31} + \gamma_{32}}{2}$, $b = i(\Delta_p + \Delta_c \pm \Delta_B) + \frac{\gamma_{43}}{2}$, $c = i(\Delta_p + \Delta_c + \Delta_d \pm \Delta_B) + \frac{\gamma_{51} + \gamma_{52} + \gamma_{54}}{2}$; the negative or positive sign before Δ_B in the expressions of a, b, and c corresponds to ρ_{31} or ρ_{32}.

In Fig. 2, we analyze the influence of the driving and the external magnetic fields on the absorption and dispersion properties of the atomic medium for the probe field in the steady-state. We can observe that in the simultaneous absence of a magnetic field and driving field, only one EIT window appears at position $\Delta_p = 0$ that created by the control field. However, in the presence of the driving field (and without magnetic field), the two EIT windows appear symmetrically over $\Delta_p = 0$ on the probe absorption profile so that the atomic medium represents maximum absorption in the resonant region and transparency in the resonant neighborhood regions [see Fig. 2(a)]. At the same time, the dispersion curve is also converted between anomalous and normal dispersions with enhanced amplitude [see Fig. 2(b)]. On the other hand, when the magnetic field is activated with B = $3\gamma_c$, which corresponds to $\Delta_B = 3\gamma$ (and without driving field), the entire absorption profile is shifted to the left for the left-circularly polarized probe beam or to the right for the right-circularly polarized probe beam, by the same amount of $\Delta_p = \Delta_B = 3\gamma$ as shown in Fig. 2(c). This means that the position of the EIT window is also shifted by the same amount $\Delta_p = 3\gamma$, so the resonant frequency region represents maximum absorption. Fig. 2(d) depicts the probe absorption spectrum in the simultaneous presence of magnetic field and driving field. In this case (for B = $3\gamma_c$), the two EIT windows appear symmetrically over $\Delta_p = -3\gamma$ for the left-circularly polarized component or $\Delta_p = +3\gamma$ for the right-circularly polarized component so
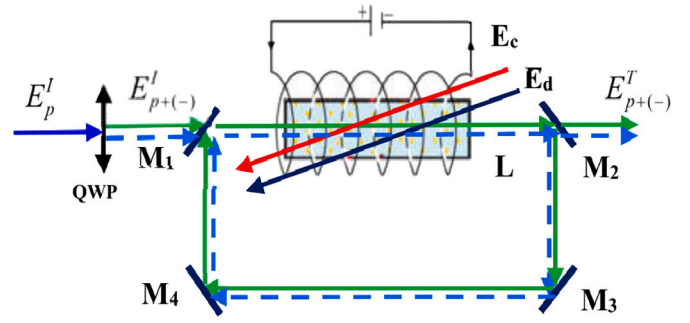
Fig. 4. The unidirectional ring cavity containing N atoms in the sample of length L, E_p^I and E_p^T is the incident and transmission fields, respectively. A static magnetic field B is applied to the sample in the direction of light propagation. Other applied fields, E_c and E_d, are non-circulating in the cavity. The solid (or dashed) line corresponds to the right (or left)-circularly polarized beams. The reflection (R) and transmission (T) coefficients of mirrors M_1 and M_2 assumed that R + T = 1 and mirrors M_3 and M_4 have perfect reflectivity.

that at these positions the absorption is maximum. This, once again, switches the maximum absorption regime to the transparency regime in the resonant region. Thus, by turning the driving field and/or the magnetic field ON or OFF, the atomic medium is also switched between EIA and EIT regimes.

To deeper understand the dependence of probe absorption on the driving field and the magnetic field, we plotted Im(ρ_{31}, ρ_{32}) versus the driving field intensity Ω_d at different values of the magnetic field, as depicted in Fig. 3. For the case when B = 0 [blue dashed line], we can see that the probe absorption coefficient increases rapidly from zero to a maximum value as the driving field intensity rises from $\Omega_d = 0$ to $\Omega_d = 3\gamma$; afterward, the probe absorption reaches a steady-state value as the intensity of the driving field continues to increase. In contrast, when B = $\pm 3\gamma_c$ [red solid line], the probe absorption coefficient decreases from a maximum value to zero as the driving field intensity rises from $\Omega_d = 0$ to $\Omega_d = 3\gamma$; and then, it gradually rises to a value greater than zero and eventually approaches a small steady-state value. Such variable absorption and dispersion properties are the physical basis for OB-OM formation and all-optical switching, which will be studied below.

3.2. Controllable optical bistability and multistability

Now, we consider the behavior of optical bistability and multistability in the $\Lambda + \Xi$-type five-level atomic system, where the sample containing N atoms is placed into a unidirectional ring cavity, as represented in Fig. 4. In this configuration, mirrors M_3 and M_4 are assumed to have perfect reflectivity, while the reflection and transmission coefficients of mirrors M_1 and M_2 are R and T (with T = 1 - R), respectively. Furthermore, here only the probe field E_p is propagated through the cavity whereas the coupling fields E_c and E_d are not, so the total electromagnetic field follows the equation: $E = E_p e^{-i\omega_p t} + E_c e^{-i\omega_c t} + E_d e^{-i\omega_d t} + c.c.,$. Under the slowly varying envelope approximation, the probe field propagation is given by:
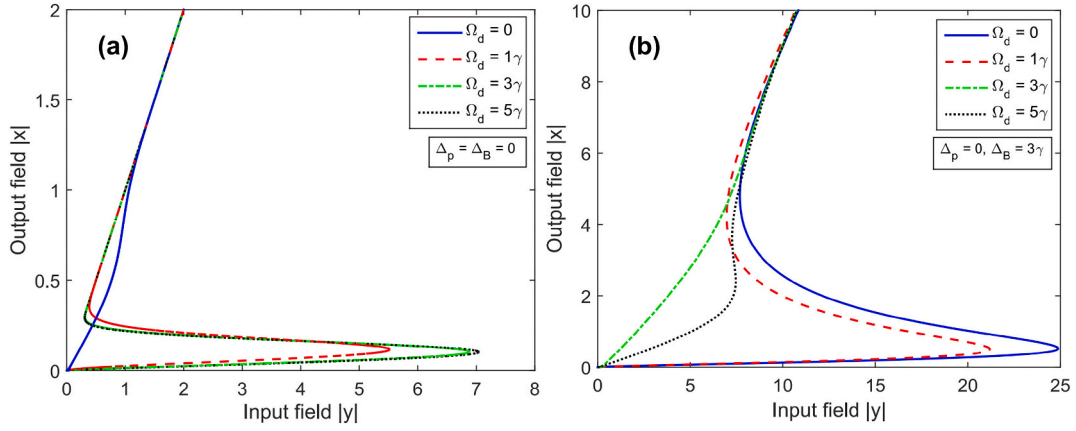
$$\frac{\partial E_p}{\partial t} + c\frac{\partial E_p}{\partial z} = i\frac{\omega_p}{2\varepsilon_0}P(\omega_p).\tag{5}$$

where c and ε_0 are the light speed and permittivity in free space, respectively, $P(\omega_p)$ is induced polarization in transitions $|3\rangle \leftrightarrow |1\rangle$ and $|3\rangle \leftrightarrow |2\rangle$:
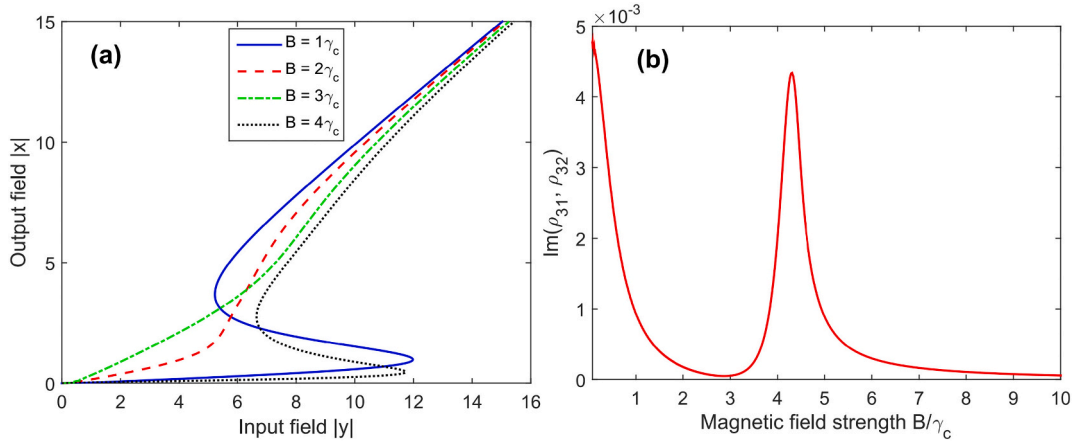
$$P(\omega_p) = N\mu(\rho_{31}, \rho_{32}).\tag{6}$$

here we assume $\mu_{31} = \mu_{32} = \mu$. From Eqs. (5) and (6), we have:

$$\frac{\partial E_p}{\partial z} = i\frac{N\mu\omega_p}{2c\varepsilon_0}(\rho_{31}, \rho_{32}).\tag{7}$$

Fig. 5. Graphs output-field versus input field at the different values of the driving field Ω_d: $\Delta_B = 0$ or $B = 0$ (a) and $\Delta_B = 3\gamma$ or $B = 3\gamma_c$ (b). The selected parameters are: $\Omega_c = 3\gamma$, $C = 200$, and $\Delta_c = \Delta_d = \Delta_p = 0$, respectively.

Fig. 6. (a) Graphs output-field versus input field at the different values of the magnetic field B. (b) Variation of the probe absorption coefficients $Im(\rho_{31}, \rho_{32})$ versus the magnetic field B. The selected parameters are: $\Omega_c = \Omega_d = 3\gamma$, $C = 200$, and $\Delta_c = \Delta_d = \Delta_p = 0$, respectively.

The boundary conditions in the steady-state limit between the input field E_p^I and the transmitted field E_p^T are as [25,28]:

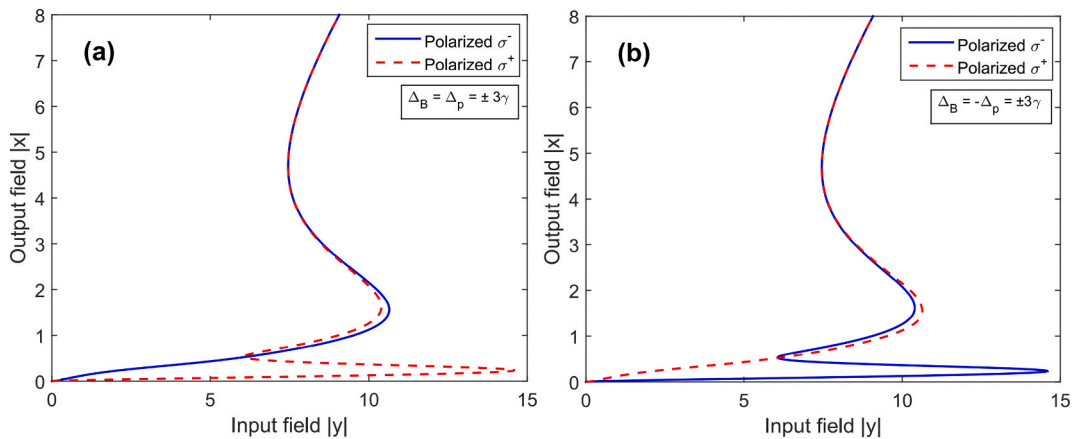$$E_p(0) = \sqrt{T}E_p^I + RE_p(L), \quad E_p(L) = E_p^T / \sqrt{T}, \tag{8}$$

The reflection mechanism of mirror M_2 causes the bistability behavior, so bistability does not occur if $R = 0$. We can obtain the input-output relationship by employing Eq. (8) and incorporating the mean-field limit and boundary conditions [25].

$$y = 2x - iC\rho_{31}, \tag{9a}$$

$$y = 2x - iC\rho_{32}, \tag{9b}$$

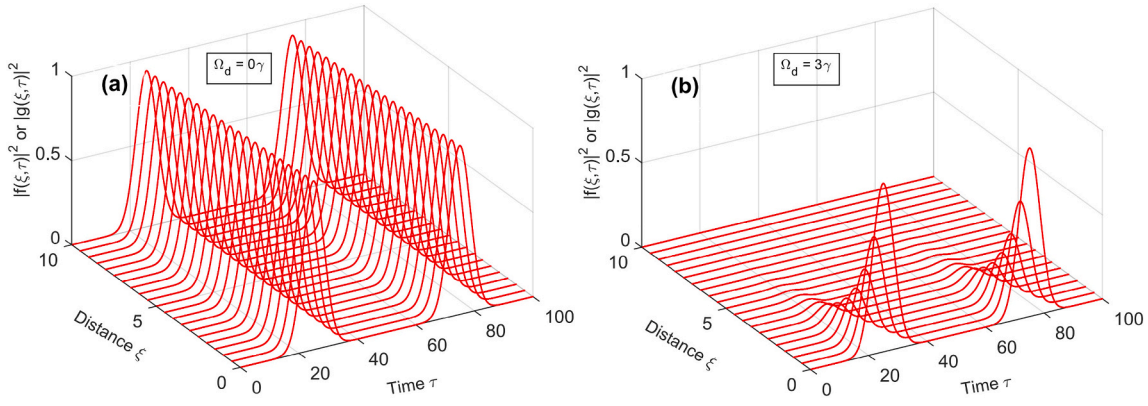where $y = \mu E_p^I / \hbar\sqrt{T}$ and $x = \mu E_p^T / \hbar\sqrt{T}$ are the normalization of the

Fig. 7. The bistability and multistability behaviors for two left and right polarization components at the $\Delta_p = \pm\Delta_B = \pm3\gamma$ (or $B = \pm3\gamma_c$). The selected parameters are: $\Omega_c = \Omega_d = 3\gamma$, $C = 200$, and $\Delta_c = \Delta_d = 0$, respectively.

Fig. 8. Space-time evolution of two circularly polarized components of the probe pulse intensity when the driving field is turned on $\Omega_d = 0$ (a) and turned off $\Omega_d = 3\gamma$ (b). The other parameters are given by $\Omega_c = 3\gamma$, $\Omega_{p0} = 0.01\gamma$, B = 0, and $\Delta_c = \Delta_d = \Delta_p = 0$, respectively.

fields, and $C = \frac{\omega_p N L |\mu|^2}{2\varepsilon_0 \hbar c T}$ is the cooperation parameter. Eqs. (9a) and (9b) shows that the coherence terms ρ_{31} and ρ_{32} have a significant role in the establishment of the OB and OM behavior of the system. So, in the following section, we numerical solving of Eqs. (3a) to (3p) in the steady-state condition and use Eqs. (9a) and (9b) to obtain the behavior of OB and OM through system parameters.

In Fig. 5 we investigate the influence of the driving field on the bistability behavior when the magnetic field is absent or present. The selected parameters are: $\Omega_c = 3\gamma$, C = 200, and $\Delta_c = \Delta_d = \Delta_p = 0$, respectively. Here, the coupling field is always on with intensity $\Omega_c = 3\gamma$, and investigations take place in the probe resonance frequency region $\Delta_p = 0$. In the case of the magnetic field is absent [Fig. 5(a)], no OB occurs when $\Omega_d = 0$ (solid line) because the medium represents the EIT regime at $\Delta_p = 0$, so the linear and nonlinear dispersions are zero [see Fig. 2(b)]; however, when the driving field is turned on and its intensity gradually increases, OB is formed because the appearance of the driving field causes the atomic medium to gradually switch from EIT to EIA regimes so that the dispersion coefficient is gradually increased, but the threshold intensity and the width of OB are also increased in EIA regime due to the strong absorption of the medium. Conversely, when the magnetic field is applied (with B = $3\gamma_c$) [Fig. 5(b)], the medium gradually changes from EIA to EIT regimes as the driving field intensity increases from $\Omega_d = 0$ to $\Omega_d = 3\gamma$ and thus, the threshold intensity and the width of OB also gradually decrease; when the driving field intensity $\Omega_d = 3\gamma$, OB also disappears because the medium is in EIT region and dispersion is zero; further increases in the driving laser intensity, OB occurs again with low threshold intensity because the absorption decreases as seen in Fig. 3 (solid line).

Next, we consider the influence of the magnetic field B on the behavior of optical bistability at $\Delta_p = 0$ and $\Omega_d = \Omega_c = 3\gamma$ as displayed in Fig. 6(a). This figure shows that no OB occurs at B = $3\gamma_c$ (dashed-dot line) because the absorption and dispersion are zero. In addition to this value of the magnetic field, OB is formed with different threshold intensity and width depending on the absorption of the medium, for example, at B = $1\gamma_c$ or B = $4\gamma_c$ the absorption coefficient is greater than that at B = $2\gamma_c$ [see Fig. 6(b)], so the threshold intensity and the width of OB are also greater respectively.

In the above cases, our investigations are displayed at the probe resonance frequency region, so the optical response of the atomic medium for two polarization components (left and right) of the probe field is identical. In Fig. 7, we consider the influence of magnetic field B on the behavior of OB when the probe detuning is non-zero, whereas other parameters are fixed at $\Omega_c = \Omega_d = 3\gamma$ and $\Delta_c = \Delta_d = 0$. The results in Fig. 7 show that optical multistability (OM) can occur for both polarization components of the probe field, specifically at $\Delta_p = \Delta_B = \pm 3\gamma$, OM appears for the right circular polarization component (dashed line), whereas the left circular polarization component still exhibits OB [see

Fig. 7(a)]; in contrast, when $\Delta_p = -\Delta_B = \pm 3\gamma$, OM is generated with the left circular polarization component (solid line), while the right circular polarization component represents OB [see Fig. 7(b)]. Thus, we can switch between OB and OM by either changing the probe light polarization (for a given magnetic field) or changing the sign of the magnetic field (for a given light polarization). The result is significant because multi-channel optical switching devices requiring multiple outputs inherit this advantage. The physical nature of these phenomena is clearly observable through the probe absorption spectrum in Fig. 2(d), specifically at $\Delta_p = 3\gamma$ and $\Delta_B = 3\gamma$, the probe absorption is enhanced corresponding to the right circular polarization component, while the left circular polarization component is reduced; the situation is the opposite when $\Delta_p = -3\gamma$. In addition, changing the sign of the magnetic field also results in a change in absorption (for a given polarization light) between the EIT and EIA regimes. Furthermore, the occurrence of optical multistability in these cases can be elucidated from the Eqs. (9a) and (9b). Notably, the variable (y) in Eqs. (9a) and (9b) does not exhibit proportionality to a cubic polynomial in the regions of the investigated parameters [25,27]. All these factors are the physical basis for the formation of OM and the transition between OB and OM that we observed in Fig. 7.

3.3. Controllable optical soliton and all-optical switching

To demonstrate and address the practical significance of the analysis provided in the previous section, we consider the propagation dynamics of the probe laser field in the $\Lambda + \Xi$-type five-level scheme under the EIT condition by deriving the one-dimensional wave propagation equation from the Maxwell wave equations in the slowly varying envelope approximation, as follows:
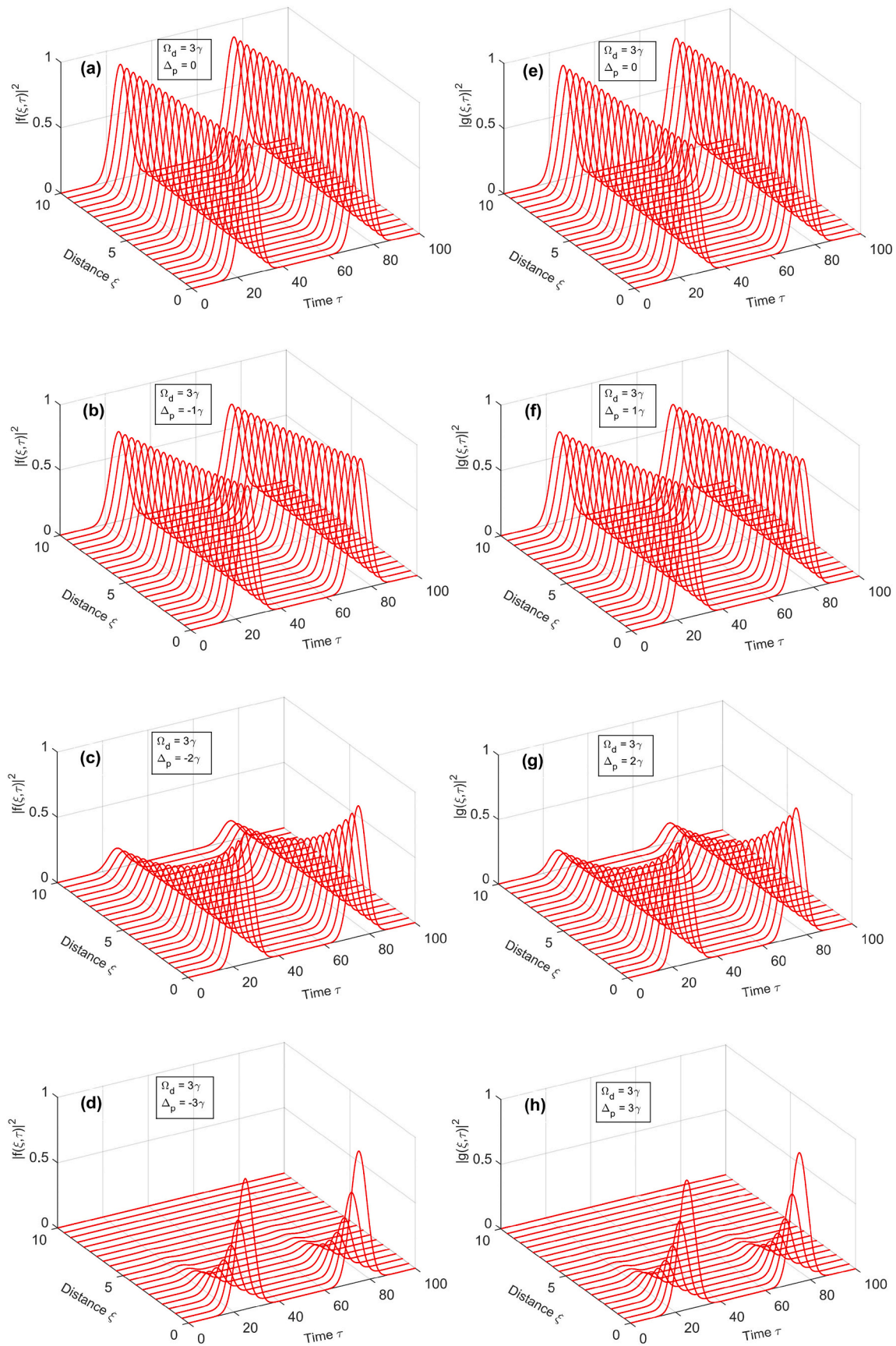
$$\frac{\partial \Omega_{p-}(z,t)}{\partial z} + \frac{1}{c}\frac{\partial \Omega_{p-}(z,t)}{\partial t} = i\alpha\rho_{31}(z,t) \tag{10a}$$

$$\frac{\partial \Omega_{p+}(z,t)}{\partial z} + \frac{1}{c}\frac{\partial \Omega_{p+}(z,t)}{\partial t} = i\alpha\rho_{32}(z,t) \tag{10b}$$

where $\alpha = \frac{\omega_p N |\mu|^2}{4\varepsilon_0 c\hbar}$ is the propagation constant. It is easier to transform the density matrix Eqs. (3a) to (3p) and the wave Eqs. (10a) and (10b) in the local frame by setting $\xi = z$ and $\tau = t - z/c$, where c is the speed of light in the vacuum. In this frame, Eqs. (3a) to (3p) will be the same with the substitution $t \rightarrow \tau$ and $z \rightarrow \xi$, while Eqs. (10a) and (10b) are rewritten as:

$$\frac{\partial \Omega_{p-}(\xi,\tau)}{\partial \xi} = i\alpha\rho_{31}(\xi,\tau) \tag{11a}$$

$$\frac{\partial \Omega_{p+}(\xi,\tau)}{\partial \xi} = i\alpha\rho_{32}(\xi,\tau) \tag{11b}$$

Fig. 9. Space-time evolution of two circularly polarized components of the probe pulse intensity at different values of probe detuning: $\Delta_p = 0$ for [panels (a) and (e)], $\Delta_p = \mp 1\gamma$ for [panels (b) and (f)], $\Delta_p = \mp 2\gamma$ for [panels (c) and (g)], $\Delta_p = \mp 3\gamma$ for [panels (d) and (h)]. The other parameters are given by $\Omega_c = \Omega_d = 3\gamma$, $\Omega_{p0} = 0.01\gamma$, $B = 3\gamma_c$, and $\Delta_c = \Delta_d = 0$, respectively.
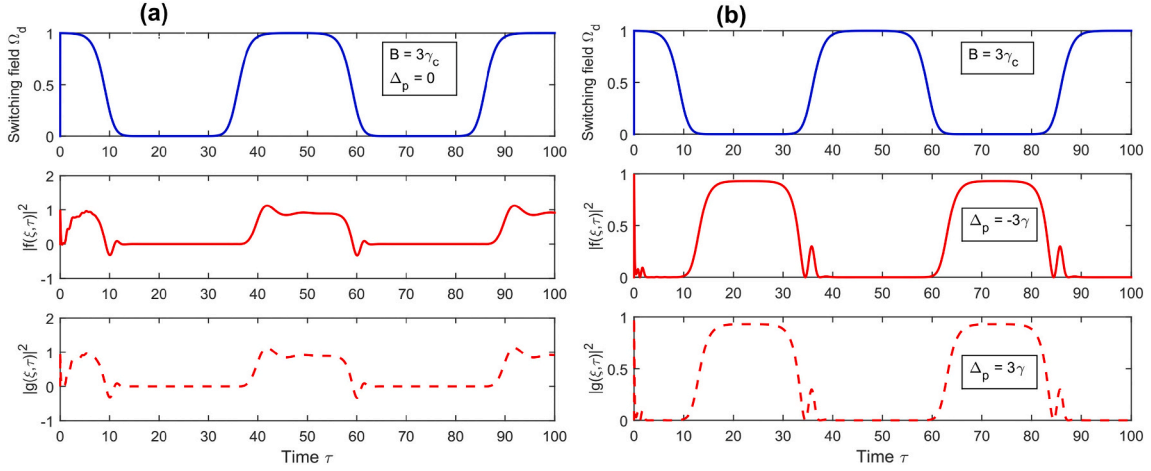
Fig. 10. Time evolution of two left-circularly polarized (red solid line) and left-circularly polarized (red dashed line) components of the probe laser field under the driving laser modulation (blue solid line) at different probe frequency detuning: $\Delta_p = 0$ (panel a) and $\Delta_p = \mp 3\gamma$ (panel-b). The other parameters are given by $\Omega_c = \Omega_d = 3\gamma$, $\Omega_{p0} = 0.01\gamma$, $B = 3\gamma_c$, and $\Delta_c = \Delta_d = 0$, respectively. (For interpretation of the references to color in this figure legend, the reader is referred to the web version of this article.)

For convenience, we represent the probe Rabi frequency by $\Omega_{p-} = \Omega_{p0} f(\xi,\tau)$, $\Omega_{p+} = \Omega_{p0} g(\xi,\tau)$, where Ω_{p0} is a real constant indicating the maximum value of the probe Rabi frequency at the entrance of the medium $\xi = 0$, and $f(\xi,\tau)$ and $g(\xi,\tau)$ are dimensionless spatiotemporal pulse-shaped function. Therefore, Eqs. (11a) and (11b) can be rewritten as:

$$\frac{\partial f(\xi,\tau)}{\partial(\alpha\xi)} = i\frac{\rho_{31}(\xi,\tau)}{\Omega_{p0}} \tag{12a}$$

$$\frac{\partial g(\xi,\tau)}{\partial(\alpha\xi)} = i\frac{\rho_{32}(\xi,\tau)}{\Omega_{p0}} \tag{12b}$$

To simulate the propagation dynamics of the probe laser field, we numerically solve the coupled Bloch-Maxwell Eqs. (3a) to (3p) and (12a) and (12b) on a space-time grid by a combination of the four-order Runge-Kutta and finite difference numerical methods with a computer code developed from previous works [28,49]. For the initial condition at which all atoms are assumed in the ground states $|1\rangle$ and $|2\rangle$, i.e., $\rho_{11}(\xi,\tau = 0) = \rho_{22}(\xi,\tau = 0) = 0.5$, and for the boundary condition at which the two left- and right-circularly polarized components of the initial probe field having a Gaussian-pulse pair shape: $f(\xi = 0,\tau) = g(\xi = 0,\tau) = exp\left[-(ln2)(\tau - 25)^2/\tau_0^2\right] + exp\left[-(ln2)(\tau - 75)^2/\tau_0^2\right]$, with $\tau_o = 6/\gamma$ being the temporal width of the pulse at the entrance of the medium.

In Fig. 8, we plot the spatiotemporal evolution of probe field intensity at different driving field intensities $\Omega_d = 0$ (a) and $\Omega_d = 3\gamma$ (b) when magnetic field is absent $B = 0$ and $\Delta_p = \Delta_c = \Delta_d = 0$. When the driving field is turned off ($\Omega_d = 0$), the atomic medium is transparent to the probe pulse, and thus the probe pulse retains its shape over a long distance as an optical soliton (Fig. 8a). When the driving field is turned on ($\Omega_d = 3\gamma$), the probe pulse is completely absorbed by the medium, even over a very short propagation distance (Fig. 8b). This phenomenon is completely consistent with the absorption or transparency behavior of the probe beam in Fig. 2(a) discussed above. Again, this demonstrates that turning the driving field on or off allows the probe pulse to be wholly transmitted or attenuated by the medium.

In Fig. 9, we plot the spatiotemporal evolution of probe field intensity with the left-circularly polarized component (a–d) and right-circularly polarized component (e–h) at different values of probe detuning when the magnetic field and driving field are applied simultaneously. At the probe detuning $\Delta_p = 0$, both circularly polarized components propagate without attenuation and have the form of optical soliton [see Fig. 9(a) and (e)] when both the magnetic field and the

driving field are turned on. However, when going outside the center frequency (i.e., $\Delta_p \neq 0$), the probe field intensity gradually decreases with the increase of probe detuning [see Fig. 9(b–c) and (f–g)] and almost completely attenuates in short distances when $\Delta_p = \mp 3\gamma$ [see Fig. 9(d) and (h)]. These behaviors are also wholly consistent with the absorption or transparency properties of the probe beam in Fig. 2(d) above. This again demonstrates that by turning the driving field on or off, the probe field can be wholly transmitted or entirely attenuated by the medium. Thus, if the driving field is modulated to a square pulse with amplitude normalized by 0 and 1, then the probe field is also modulated accordingly. It will be indicated in Fig. 10 below.

Finally, in order to inspect the switching of the probe field (left- and right-circularly polarized components) in terms of the driving field, we assume that the probe field is a continuous wave (cw) and the driving field is modulated by a near square pulse of the form: $\Omega_d(\tau) = \Omega_{d0}\{1 - 0.5\tanh[0.4(\tau - 10)] + 0.5\tanh[0.4(\tau - 35)] - 0.5\tanh[0.4(\tau - 60)] + 0.5\tanh[0.4(\tau - 85)]\}$ with an approximate period $50/\gamma$. In Fig. 10, we plot the time evolution of the probe laser field at different probe detuning positions: $\Delta_p = 0$ for panel (a) and $\Delta_p = \mp 3\gamma$ for (b) by fixing the laser parameters at $f(\xi = 0,\tau) = g(\xi = 0,\tau) = 1$, $\Omega_c = \Omega_{d0} = 3\gamma$, $\Omega_{p0} = 0.01\gamma$, $B = 3\gamma_c$ and $\Delta_c = \Delta_d = 0$. As depicted in Fig. 10, it demonstrates that the probe field (continuous wave) has been switched to a near square pulse train versus modulation (ON or OFF) of the driving field. Specifically, at $\Delta_p = 0$, the twin probe pulses are switched synchronously with the pulse modulation of the driving field [panel (a)]. However, at $\Delta_p = \mp 3\gamma$, the twin probe pulses are switched antisynchronously with the driving pulse [panel (b)]. This behavior can be explained by the fact that in the presence or absence of the driving field under the magnetic field, the main EIT window (central dip) and the two sideband EIT windows (sideband dips) will shift left or right, as shown in Fig. 2(c) and (d). As a result, this ($\Lambda + \Xi$) five-level atomic system can be utilized for achieving dual all-optical switching of the weak probe field by modulating the driving field.

4. Conclusion

To summarize, we have demonstrated optical bistability, optical multistability, optical soliton and dual all-optical switching in a $\Lambda + \Xi$-type five-level EIT medium by utilizing an external magnetic field and applied laser fields. The results indicate that adjusting the magnetic field strength and driving field can manipulate the threshold and width of the optical bistability in different spectral regions of the probe field. Moreover, by varying the intensity/sign of the magnetic field in the presence

of the driving field, it requires almost no effort to switch between optical bistability and optical multistability. Notably, we have achieved steady propagation of weak twin probe pulses and performed dual all-optical switching simultaneously. This proposed model holds the potential to enable multi-channel all-optical switching and optical storage, making it suitable for various applications in optical communications.

CRediT authorship contribution statement

Hoang Minh Dong: Data curation, Formal analysis, Investigation, Methodology, Software, Supervision, Writing – original draft, Writing – review & editing. **Nguyen Thi Thu Hien:** Data curation, Formal analysis, Investigation. **Nguyen Huy Bang:** Conceptualization, Methodology, Supervision, Writing – review & editing. **Le Van Doai:** Conceptualization, Formal analysis, Investigation, Methodology, Project administration, Supervision, Writing – original draft.

Declaration of competing interest

The authors declare that they have no known competing financial interests or personal relationships that could have appeared to influence the work reported in this paper.

Data availability

No data was used for the research described in the article.

Acknowledgment

References

[1] Li Baojun, Chua Soo Jin. Optical switches: materials and design. Woodhead Publishing Limited; 2010.

[2] Fleischhauer M, Imamoglu A, Marangos JP. Electromagnetically induced transparency: optics in coherent media. Rev Mod Phys 2005;77:633.

[3] El-Nabulsi RA, Anukool W. A family of nonlinear Schrodinger equations and their solitons solutions. Chaos Solit Fractals 2023;166:112907.

[4] Zhou R, Hao H, Jia R. New soliton solutions for the (2+1)-dimensional Schrödinger-Maxwell-Bloch equation. Superlattices Microstruct 2018;113:409–18.

[5] Jia R-Rong, Guo R. Breather and rogue wave solutions for the (2+1)-dimensional nonlinear Schrödinger-Maxwell-Bloch equation. Appl Math Lett 2019;93:117–23.

[6] Qing-Chun JI. Darboux transformation and solitons for reduced Maxwell Bloch equations. Commun Theor Phys 2005;43:983.

[7] Wang R-Ru, Wang Y-Yue, Dai C-Qing. Dissipative solitons of the nonlinear fractional Schrodinger equation with PT-symmetric potential. Optik 2022;254:168639.

[8] Boller KJ, Imamoglu A, Harris SE. Observation of electromagnetically induced transparency. Phys Rev Lett 1991;66:2593.

[9] Thanh TD, Anh NT, Hien NTT, Dong HM, Hao NX, Khoa DX, et al. Subluminal and superluminal light pulse propagation under an external magnetic field in a vee-type three-level atomic medium. Photonics Lett Pol 2021;13(1):4–6.

[10] Wang H, Goorskey D, Xiao M. Enhanced Kerr nonlinearity via atomic coherence in a three-level atomic system. Phys Rev Lett 2001;87:073601.

[11] Dong HM, Anh NT, Thanh TD. Controllable Kerr nonlinearity in a degenerate V-type inhomogeneously broadening atomic medium aided by a magnetic field. Opt Quantum Electron 2022;54(4):225.

[12] Mu Y, Qin L, Shi Z, Huang G. Giant Kerr nonlinearities and magneto-optical rotations in a Rydberg-atom gas via double electromagnetically induced transparency. Phys Rev A 2021;103:043709.

[13] Harris SE, Hau LV. Nonlinear optics at low light levels. Phys Rev Lett 1999;82:4611.

[14] Hau LV, Harris SE, Dutton Z, Bejroozi CH. Light speed reduction to 17 meters per second in an ultracold atomic gas. Nature 1999;397:594–8.

[15] Venkataraman V, Saha K, Gaeta AL. Phase modulation at the few-photon level for weak-nonlinearity-based quantum computing. Nat Photon 2013;7:138–41.

[16] Joshi A, Xiao M. Controlling steady-state and dynamical properties of atomic optical Bistability. World Scientific; 2012.

[17] Gong S, Du S, Xu Z. Optical bistability via atomic coherence. J Phys Lett A 1997;226:293–7.

[18] Harshawardhan W, Agarwal GS. Controlling optical bistability using electromagnetic-field-induced transparency and quantum interferences. Phys Rev A 1996;53:1812.

[19] Brown A, Joshi A, Xiao M. Controlled steady-state switching in optical bistability. Appl Phys Lett 2003;83:1301.

[20] Joshi A, Yang W, Xiao M. Effect of quantum interference on optical bistability in the three-level V-type atomic system. J Phys Rev A 2003;68:015806.

[21] Jafarzadeh H, Sahrai M, Ghaleh K. Controlling the optical bistability in a Λ-type atomic system via incoherent pump field. Appl Phys B 2014;117:927–33.

[22] Dong HM, Thanh TD, Hien NTT, Nga LTY, Bang NH. Controlling optical switching by an external magnetic field in a degenerate vee-type atomic medium. Phys Lett A 2023;469:128765.

[23] Cheng D, Liu C, Gong S. Optical bistability and multistability via the effect of spontaneously generated coherence in a three-level ladder-type atomic system. J Phys Lett A 2004;332:244–9.

[24] Haifeng X. Optical bistability and multistability via both coherent and incoherent fields in a three-level system. Laser Phys 2019;29:015205.

[25] Asadpour SH, Eslami-Majd A. Controlling the optical bistability and transmission coefficient in a four-level atomic medium. JOL 2012;132:1477–82.

[26] Zhang D, Yu R, Li J, Ding C, Yang X. Laser-polarization-dependent and magnetically controlled optical bistability in diamond nitrogen-vacancy centers. Phys Lett A 2013;377:2621.

[27] Anh NT, Hien NTT, Thanh TD, Doai LV, Khoa DX, Bang NH, et al. External magnetic field-assisted polarization-dependent optical bistability and multistability in a degenerate two-level EIT medium. Laser Phys Lett 2023;20:035201.

[28] Dong HM, Nga LTY, Bang NH. Optical switching and bistability in a degenerated two-level atomic medium under an external magnetic field. Appl Optics 2019;58(16). 4192-1499.

[29] Li YN, Chen YY, Wan RG, Yan HW. Dynamical switching and memory via incoherent pump assisted optical bistability. Phys Lett A 2019;383:2248.

[30] Chakravarty S. Soliton solutions of coupled Maxwell–Bloch equations. Phys Lett A 2016;380:1141–50.

[31] Harris SE, Luo Zhen-Fei. Preparation energy for electromagnetically induced transparency. Phys Rev A 1995;52:R928.

[32] Dong HM, Doai LV, Sau VN, Khoa DX, Bang NH. Propagation of laser pulse in a three-level cascade atomic medium under conditions of electromagnetically induced transparency. Photonics Lett Pol 2016;8:73.

[33] Khoa DX, Dong HM, Doai LV, Bang NH. Propagation of laser pulse in a three-level cascade inhomogeneously broadened medium under electromagnetically induced transparency conditions. Optik 2017;131:497.

[34] Dong HM, Doai LV, Bang NH. Pulse propagation in an atomic medium under spontaneously generated coherence, incoherent pumping, and relative laser phase. Opt Commun 2018;426:553.

[35] Dong HM, Nga LTY, Khoa DX, Bang NH. Controllable ultraslow optical solitons in a degenerated two-level atomic medium under EIT assisted by a magnetic field. Sci Rep 2020;10(1):15298.

[36] Chen Y, Bai Z, Huang G. Ultraslow optical solitons and their storage and retrieval in an ultracold ladder-type atomic system. Phys Rev A 2014;89:023835.

[37] Schmidt H, Ram RJ. All-optical wavelength converter and switch based on electromagnetically induced transparency. Appl Phys Lett 2000;76:3173.

[38] Yavuz DD. All-optical femtosecond switch using two-photon absorption. Phys Rev A 2006;74:053804.

[39] Antón MA, Carreño F, Calderón OG, Melle S, Gonzalo I. Optical switching by controlling the double-dark resonances in a N-tripod five-level atom. Opt Commun 2008;281:6040–8.

[40] Yu R, Li J, Huang P, Zheng A, Yang X. Dynamic control of light propagation and optical switching through an RF-driven cascade-type atomic medium. Phys Lett A 2009;373:2992.

[41] Fountoulakis A, Terzis AF, Paspalakis E. All-optical modulation based on electromagnetically induced transparency. Phys Lett A 2010;374:3354–64.

[42] Qi Y, Niu Y, Zhou F, Peng Y, Gong S. Phase control of coherent pulse propagation and switching based on electromagnetically induced transparency in a four-level atomic system. J Phys B At Mol Opt Phys 2011;44:085502.

[43] Qi Y, Zhou F, Yang J, Niu Y, Gong S. Controllable twin laser pulse propagation and dual-optical switching in a four-level quantum dot nanostructure. J Opt Soc Am B 2013;30:1928.

[44] Yu R, Li J, Ding C, Yang X. Dual-channel all-optical switching with tunable frequency in a five-level double-ladder atomic system. Opt Commun 2011;284:2930.

[45] Ma J, Yang X, Huang M, Liang X, Deng D, Liu H, et al. All-optical switch with ultrahigh switching efficiency and ultralow threshold energy based on a one-dimensional PT-symmetric ring optical waveguide network. Commun Nonlinear Sci Numer Simul 2023;118:106990.

[46] Dong HM, Bang NH. Controllable optical switching in a closed-loop three-level lambda system. Phys Scr 2019;94:115510.

[47] Anh NT, Thanh TD, Bang NH, Dong HM. Microwave assisted all-optical switching in a four-level atomic system. Pramana J Phys 2021;95:37.

[48] Khoa DX, Ai NV, Dong HM, Doai LV, Bang NH. All-optical switching in a medium of a four-level vee-cascade atomic medium. Opt Quantum Electron 2022;54(3):164.

[49] Dong HM, Bang NH, Khoa DX, Doai LV. All-optical switching via spontaneously generated coherence, relative phase and incoherent pumping in a V-type three-level system. Opt Commun 2022;507:127731.

[50] Hien NTT, Anh NT, Bang NH, Khoa DX, Doai LV, Quang HH, et al. Phase control of all-optical switching based on spontaneously generated coherence in a three-level Λ-type atomic system. Eur Phys J D 2022;76:215.

[51] Steck DA. ^{87}Rb D line data. http://steck.us/alkalidata; 2019.